修士論文

Estimation of rice plant coverage using Sentinel-2 based on UAV-observed data

令和 5 年度 修了

三重大学 大学院工学研究科 情報工学専攻

データサイエンス研究室

佐藤 優気

Abstract

Vegetation coverage is a crucial parameter in agriculture, as it offers essential insights into crop growth and health conditions. The spatial resolution of spaceborne sensors is relatively limited, making it challenging to precisely measure vegetation coverage. Consequently, fine-resolution ground observation data becomes indispensable for establishing the correlation between remotely sensed reflectance and plant coverage. This study estimated rice plant coverage per pixel using time series Sentinel-2 Multispectral Instrument (MSI) data, which enables monitoring rice growth conditions over a wide area. Rice plant coverage was calculated using Unmanned Aerial Vehicle (UAV) data with a spatial resolution of 3 cm based on the spectral unmixing method. This plant coverage map was generated every two to three weeks throughout the rice growing season. Subsequently, the plant coverage was estimated at a 10 m resolution through the multiple linear regression, utilizing Sentinel-2 MSI reflectance data and these plant coverage maps. In this process, a geometric registration of MSI and UAV data was conducted to improve their spatial agreement. The coefficient of determination (R^2) of the multiple linear regression model was 0.92 and 0.94 for the Level-1C and Level-2A products of Sentinel-2 MSI, respectively. The root mean squared error (RMSE) of the estimated rice plant coverage was 10.77% and 9.34%, respectively. This study highlights the potential of a satellite time series model for accurate estimation of rice plant coverage.

Keywords:
unmanned aerial vehicle (UAV); Sentinel-2 multispectral instrument (MSI); paddy field; rice plant coverage; mixed pixel analysis.

Glossary

Diffuse reflectance standard panel: The reference panel used in optics and imaging for consistent, diffuse reflection (Fig. A-1 in Appendix). It is crucial for the calibration and evaluation of optical devices and color measurements.

Mie no Yume: Mie Prefecture's original rice variety, which is characterized by medium maturation and exceptional eating quality.

Orthorectification: The process of removing distortions caused by terrain variations from aerial or satellite images, ensuring an accurate representation of ground features. It involves geometric correction to align the image with a map projection, enhancing its suitability for precise analysis and mapping applications.

Radiometric calibration: The process of adjusting the brightness values in remote sensing images to ensure consistency and accuracy across different sensors or over time. It enables quantitative analysis and comparison of pixel values for scientific and practical applications such as land cover mapping and environmental monitoring.

Real-time kinematic global navigation satellite system (RTK-GNSS): The precise navigation technique to enhance the positioning accuracy of GNSS data, that is used in real-time applications such as surveying, mapping, and precision agriculture. It utilizes carrier phase measurements from multiple GNSS satellites and a reference station to achieve centimeter-level positioning, enabling high-precision location-based tasks.

Unmanned Aerial Vehicle (UAV): The aircraft operated without a human pilot on board, controlled either autonomously by onboard computers or remotely by a human operator.

Yamada Nishiki: The rice variety for a premium Japanese sake. It is highly prized for its large grains, high starch content, and ability to produce high-quality sake with a delicate and refined flavor.

Table of Contents

1. Introduction

In Japanese agriculture, the number of farmers has decreased from approximately 2.337 million in 2000 to 1.028 million in 2020 [1,2]. The average age of agricultural workers was 67.8 years old in 2020 [2]. The decrease and aging of the workers is a major problem in Japanese agriculture. There is also the problem of abandoned farmland. To solve these problems, the local government has been promoting the consolidation and agglomeration of farmlands. The consolidation of farmlands accelerated in 2014 with the establishment of the Agricultural Land Bank. As a result, the consolidation rate in FY2021 was 58.9%. In addition, the number of new agricultural corporations has been steadily increasing [3–5]. As these trends indicate, the scale of agricultural management has increased. This means that agricultural efficiency is required more than ever.

The Japanese government has accelerated the social implementation of smart agriculture by launching the "Agricultural Demonstration Project" in 2019 [6]. The characteristics of smart agriculture technology basically consist of Information and Communication Technology, Robotics Technology, and Artificial Intelligence [7]. These technologies are expected to dramatically improve productivity through work automation and data sensing technology. Satellites and aircraft have been used in agricultural remote sensing. Meanwhile, the unmanned aerial vehicle (UAV) has attracted a lot of attention in recent years. UAVs are expected to be used for detailed observation of the field because they have high spatial resolution and flexible observation capabilities [8]. Kaminishi et al. [9] surveyed rice farming corporations about their future intention to adopt smart agriculture and concluded that they were highly positive about using drones and satellites to measure crop growth conditions.

Satellite remote sensing has been utilized for large-scale field data collection [10–13]. Franch et al. [14] proposed a yield prediction model that combines spectral reflectance targeting two rice varieties (JSendra and Bomba). The field-based yield forecast error during the rice tillering stage was 3.73% for JSendra and 5.82% for Bomba, respectively. Additionally, they demonstrated that the correlation between the spectral reflectance of Sentinel-2 and rice yield varied depending on the variety and phenology.

These findings emphasize the necessity of discriminating between varieties to develop satellite-based yield models. Zhao et al. [15] used spectral reflectance from the FORMOSAT-2 multispectral data with eight-meters resolution to estimate agronomic variables (biomass, leaf area index, plant nitrogen concentration, and plant nitrogen uptake). The results revealed that the regression model's performance was significantly influenced by the rice growth stage. They concluded that optimized band selection for each growth stage is crucial. Their study categorized the phenological stages into tillering, booting, and heading. Due to variations in growing environments, such as varieties and growth stages, estimations tend to be dependent on specific conditions. Constructing a generic model capturing the growth conditions of each field on a regional scale proves challenging.

Vegetation coverage in a unit area serves as a crucial parameter in various model analyses. This metric intuitively captures field conditions and minimizes the need for consideration of varieties or regional differences. In remote sensing, agricultural variables, including vegetation coverage, are frequently estimated through regression analysis using spectral reflectance and vegetation indices as parameters. However, this method necessitates validation data with true values, often acquired through manual field data collection by researchers [16–18]. Hayashi et al. [19] employed a method to estimate rice plant coverage by binarizing infrared photographs taken from a height of three meters using an elevated work vehicle. Lee et al. [20] developed a technique to isolate paddy rice from the background by calculating color indices from RGB information in digital camera images captured from a height of two meters. While these studies efficiently provide coverage information, they take time and effort in large areas. UAV has revolutionized spatial data acquisition, offering near-true values over expansive areas. With a spatial resolution surpassing that of satellites by a few centimeters, UAVs can contribute to the efficient measurement of vegetation coverage by low-altitude remote sensing and address previous challenges, such as data scarcity in the field.

In recent years, research has increasingly combined UAVs with satellite data, yielding effective results across various agricultural applications. Jiang et al. [21] focused on estimating plant dry matter (PDM) and plant nitrogen accumulation (PNA) from Sentinel-2 images. They constructed an

estimation model by investigating the optimal machine learning algorithm, incorporating satellite spectral indices, weather variables, and PDM or PNA calculated from UAV images. Schiefer et al. [22] aimed to estimate the fractional cover of standing deadwood using a Long Short-Term Memory network (LSTM) based on Sentinel-1 and Sentinel-2 time series. UAV images, segmented with standing deadwood, were employed as spatial reference data, enhancing the accuracy of the estimation model. In the study by Lewis et al. [23], the focus was on estimating the coverage of intertidal brown canopy-forming macroalgae. UAV image pixels were classified using the brown algae index (BAI) with a threshold value to calculate the coverage. Subsequently, a regression model was constructed utilizing the calculated coverage and the BAI obtained from Sentinel-2 images. These research endeavors collectively underscore the synergistic capabilities of UAVs and Sentinel-2 satellite data, showcasing their potential for accurate and detailed spatial analysis in diverse environmental and agricultural contexts.

In the realm of remote sensing technology applied to field science, the "mixed pixel problem" poses a significant challenge for many researchers. This issue arises when the land surface corresponding to a single pixel comprises multiple components, while the pixel itself holds only one spectral information. Mixed pixels encompass diverse properties, differing from pure pixels [24]. Despite hindering accurate feature detection and vegetation classification, many studies often assume that a pixel comprises a single land cover component to simplify the analysis. A method employed to address this problem is linear spectral unmixing [25,26]. In this approach, components such as plants, soil, and water in a pixel are referred to as endmembers. The observed reflectance of the mixed pixel can be expressed as a linear combination of the pure reflectance of these endmembers and their respective area fractions. This technique enables the estimation of the area fraction corresponding to each component within a pixel. By employing linear spectral unmixing, researchers can mitigate the challenges associated with mixed pixels and enhance the accuracy of their remote sensing analyses. UAV images, owing to their fine resolution, contain more pixels compared to satellite images of the same extent. Consequently, the number of components within a single pixel decreases, while the number of pixels with distinct component boundaries increases. Despite the enhanced resolution, the consideration of mixed pixels in UAV images remains necessary. Duan

et al. [27] successfully employed the spectral unmixing method in UAV remote sensing images to calculate wheat plant coverage. This method exhibited significantly improved accuracy compared to the support vector machine and thresholding methods.

The objective of this study is to estimate rice plant coverage using Sentinel-2 Multispectral Instrument (MSI) data. In the model construction, a time series of UAV-observed plant coverage maps is generated based on the spectral unmixing method. These coverage maps serve as reference data for multiple linear regression with MSI reflectance data. Two types of MSI products, Level-1C (top-of-atmosphere reflectance) and Level-2A (atmospherically corrected surface reflectance), were utilized to evaluate estimation accuracy. Additionally, geometric registration of UAV and MSI data is conducted to improve their spatial agreement. The outcomes of this study have the potential to provide continuous plant coverage, serving as fundamental data for vegetation growth estimation.

2. Materials

2.1 Study Field

The study was conducted at Tsuji Farm, located in Tsu City, Mie Prefecture, Japan (136°29’E, 34°46’N) (Figure 1). Eight paddy field plots of Japonica rice were selected for the study. The rice variety "Mie no Yume" was cultivated in six plots (A, B, C, D, E, and F), and "Yamada Nishiki" was cultivated in two plots (G and H). "Mie No Yume" was planted on June 16 and 17, 2023. "Yamada Nishiki" was planted on May 30 and 31, 2023. The model was developed and assessed using data from the "Mie no Yume". In contrast, the "Yamada Nishiki" was used to assess the applicability of the model to other varieties.

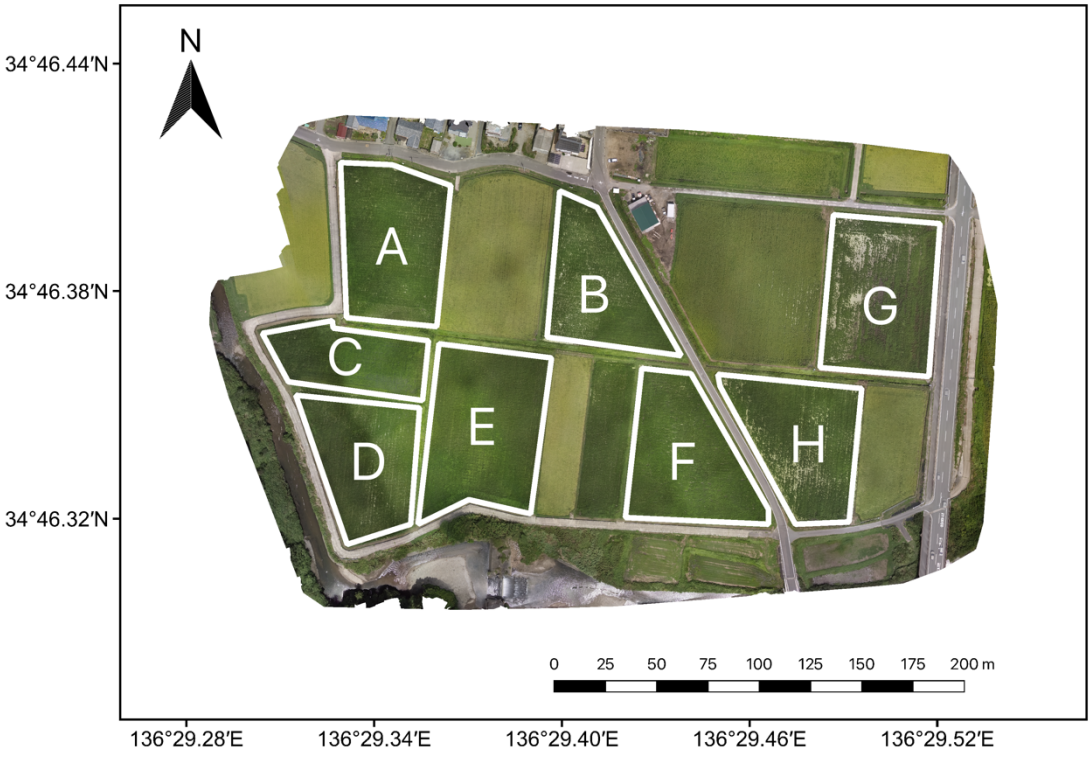

Figure 1. The study fields. Labels A to H represent the study plot.

2.2 UAV Spectral Images

We used P4 Multispectral [28], equipped with a five-band multispectral camera capturing blue to near-infrared (NIR) wave regions shown in Table 1. The camera specifications are detailed in Table 1. Flight altitude was 60 meters from the ground, and photos were obtained in equal time interval shooting mode with a 70% overlap and 90% sidelap using DJI Ground Station Pro [29] software. For radiometric calibration, a diffuse reflectance standard panel [30] was captured before take-off. Observations were carried out under varying weather conditions, encompassing both sunny and cloudy scenarios, with low wind speeds. The dates of UAV observations are provided in Table 3. The UAV images were obtained six times after rice planting to the flowering stage (Fig. A-2 in Appendix).

Table 1. Technical specifications of P4 multispectral UAV.

Specification		Value
Dimension		35 cm (diagonal size)
Take-off weight		1487 g
Image size		1600 × 1300 pixel
GSD * on 60m flight altitude		approximately 3.2 cm
Field of view		62.7 °
The spectral range of the band	Blue	456 ± 16 nm
	Green	560 ± 16 nm
	Red	650 ± 16 nm
	Rededge	730 ± 16 nm
	NIR	840 ± 26 nm

* Grand Sampling Distance

2.3 Sentinel-2 Reflectance Image

Sentinel-2 MSI was used in this study because it has higher temporal (5 days) and spatial (10 meters) resolution. Among the 13 spectral bands of MSI, we used bands 2, 3, 4, and 8 (Table 3), considering the compatibility with UAV. Both top-of-atmosphere reflectance in the Level-1C product and atmospherically corrected reflectance in the Level-2A product were examined for the comparison of model accuracy. The cloud-free data closest to the UAV observations were downloaded through the Copernicus Open Access Hub [31]. Unfortunately, Sentinel-2 data corresponding to UAV observations on September 2, 2023, could not be derived due to cloud coverage. The observation dates of the Sentinel-2 data are listed in Table 3.

Table 2. Technical specifications of Sentinel-2/MSI observations.

Specification	**Value**		
Observation width	290 km		
Observation frequency	5 days (by the combination of Sentinel-2A/2B)		
The central wavelength of the band and resolution	Band 2 (Blue)	490 nm	10 m
	Band 3 (Green)	560 nm	10 m
	Band 4 (Red)	665 nm	10 m
	Band 8 (NIR)	842 nm	10 m

Table 3. Data and time of UAV and Sentinel-2/MSI observations.

UAV	**Sentinel-2/MSI**
10:40 ~ 11:20 on June 16, 2023	10:37:01 on June 19, 2023
10:40 ~ 11:20 on June 26, 2023	10:36:59 on July 4, 2023
10:35 ~ 11:20 on July 14, 2023	10:36:59 on July 24, 2023
10:35 ~ 11:20 on July 27, 2023	10:37:01 on July 29, 2023
10:50 ~ 11:30 on August 17, 2023	10:36:59 on August 13, 2023
11:20 ~ 12:00 on September 2, 2023	-

3. Methods

A comprehensive overview of the methodologies, data handling, and procedural steps employed in this study is presented in Figure 2. The illustration encapsulates the entire process flow, illustrating how the data were utilized throughout the study.

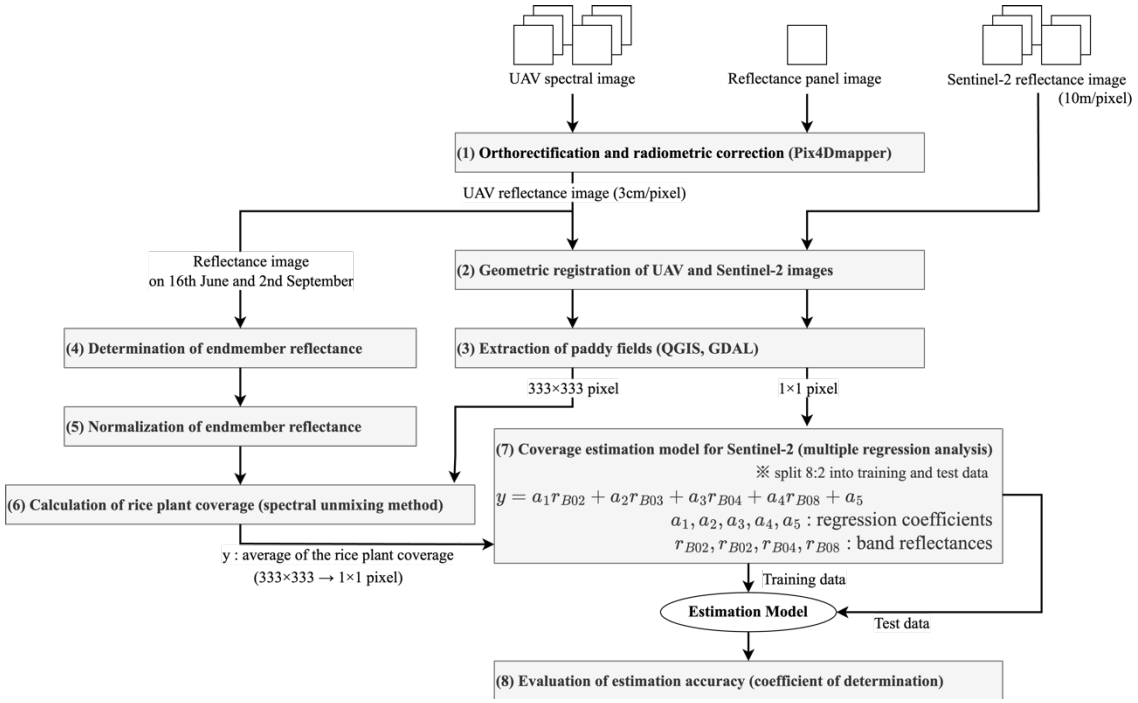

Figure 2. Flowchart of the methodology employed in this study.

3.1 Preprocessing

3.1.1 Orthorectification and Radiometric Correction

The UAV-acquired images were processed using Pix4Dmapper [32] software to generate single-band ortho reflectance images with a spatial resolution of 0.03 m. Radiometric correction was executed with the aid of a calibrated reflectance panel. It is crucial to note that the pixel values in the original images are relative to the specific conditions during data collection and are not absolute. This discrepancy is primarily attributed to variations in light conditions, such as atmospheric conditions and the sun position on the day of acquisition. Given that UAVs observe crops multiple times, achieving accurate pixel values becomes imperative. Therefore, compensating for variations in illumination conditions that impact the data, known as radiometric correction [33], is essential for enhancing the precision of the acquired information.

3.1.2 Geometric Registration of UAV and Sentinel-2 Images

The goal of this study is to estimate rice plant coverage from Sentinel-2 images at a per-pixel level. Therefore, establishing the positional relationship between UAV and Sentinel-2 images is crucial for accurate pixel comparison. It should be noted that Sentinel-2 images exhibit slight deviations from actual positions due to their 10-meter resolution. The absolute geolocation of Sentinel-2 is at least six meters [34]. In contrast, the UAV image resolution is three centimeters. Nevertheless, since RTK-GNSS was not used during the observation, the UAV images also exhibit slight deviations. Consequently, the geometric registration pre-processing step is indispensable to ensure high estimation accuracy.

Figure 3 illustrates a schematic diagram of the geometric registration process. In Figure 3a, a UAV image (blue-shaded layer) is overlaid on a Sentinel-2 image. The geometric registration process proceeded as follows:

1. The UAV image was systematically shifted, with a maximum shift of 9.0 m and increments of 0.6 m in both the north-south and west-east directions from the initial position, where it was overlaid without any

processing (Figure 3a).

2. The shifted UAV image within the red box was then clipped and scaled down to match the Sentinel-2 resolution (10 meters/pixel) by pixel averaging.

3. The correlation between the Sentinel-2 image within the red box (Figure 3b) and the scaled-down UAV image (Figure 3c) was calculated. The resulting correlation coefficients were employed to assess geometric registration accuracy.

These processes were applied to all corresponding band images. In the example depicted in Figure 3, the UAV image represents the NIR band from June 16, 2023, and the Sentinel-2 image corresponds to band 8 (NIR) from June 19, 2023. This geometric registration approach was consistently applied to all dates listed in Table 3.

For the assessment of geometric registration accuracy, we utilized green and NIR reflectance images as they exhibited a distinct trend in correlation coefficients. The geometric registration process results with higher correlation coefficients between these two band images were adopted. Notably, a higher correlation coefficient was observed in the NIR band when the rice plants were in their early growth stage. Conversely, during the later growth stage, the green band exhibited a higher correlation coefficient. This trend can be attributed to the changing proportions of paddy fields in the geometric registration target area, influencing reflectance as rice plants mature.

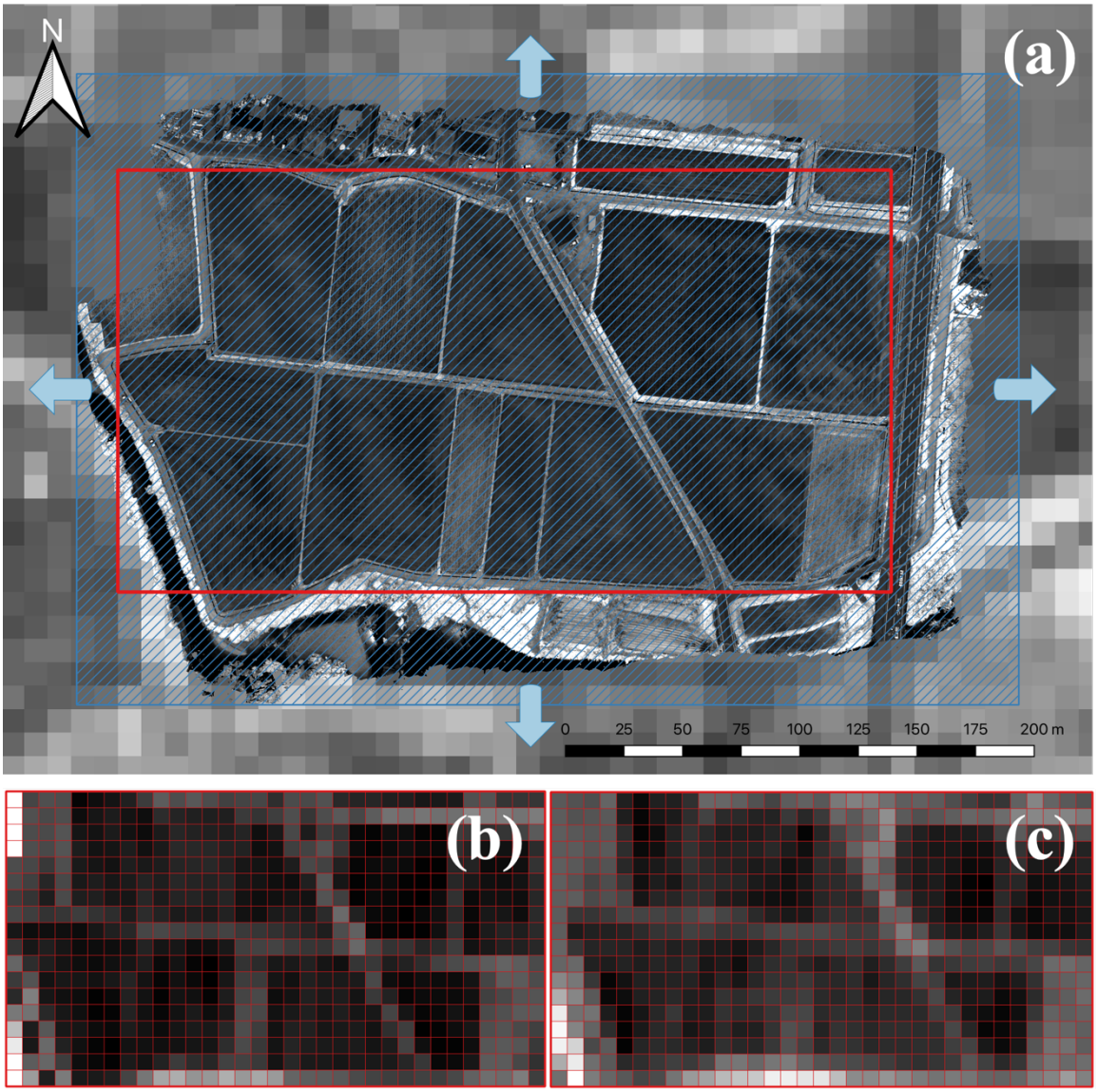

Figure 3. Geometric registration process of UAV and Sentinel-2 images. (a) Schematic diagram of the geometric registration process. (b) Downscaled UAV NIR image. (c) Sentinel-2 band8 image.

3.1.3 Extraction of Paddy Fields

Given that the focus of this study is on paddy fields, the extraction process exclusively isolates paddy field pixels using QGIS software [35] after the geometric registration process. The extraction process unfolded as follows:

1. Paddy field pixels were manually selected within the 10-meter grid depicted in Figures 3b and 3c.

2. UAV and Sentinel-2 images corresponding to the selected pixels were then extracted. The size of the extracted UAV image is 333 × 333 pixels, while the extracted Sentinel-2 image is 1 × 1 pixel.

Figure 4 illustrates the extracted pixels in both UAV and Sentinel-2 images. Due to the geometric registration processing preceding extraction, the positions of paddy field pixels varied depending on the image date. Consequently, extracted pixels, including those from non-paddy field areas, were manually excluded from further analysis.

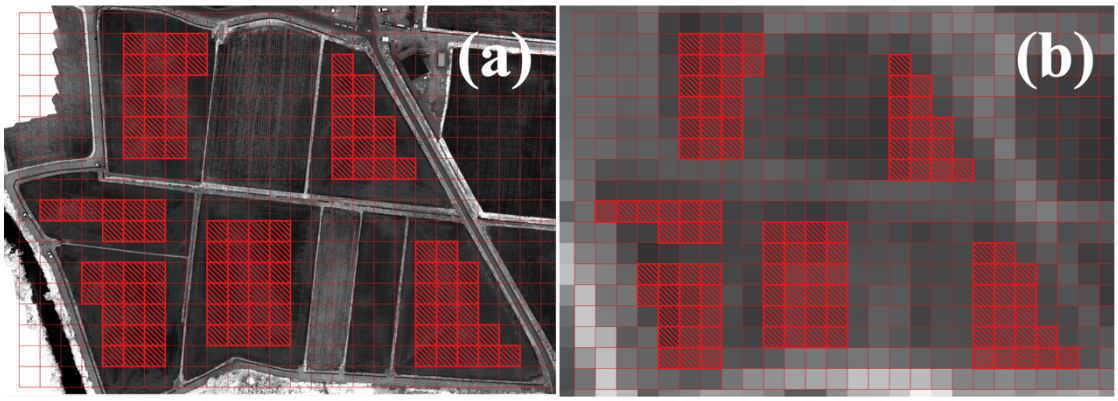

Figure 4. Extraction of paddy field pixels can be expressed as follows: (a) UAV image on 16 June 2023. (b) Sentinel-2 image on 19 June 2023.

3.2 Calculation of Rice Plant Coverage from UAV Data

3.2.1 The Linear Spectral Unmixing Method

The paddy field pixels extracted through pre-processing constitute mixed pixels containing both rice and water components. The endmembers in this context are water and rice. Consequently, the observed reflectance of the mixed pixel can be mathematically expressed as a linear combination of the pure reflectance values of the endmembers and their respective area fractions. To facilitate this, the study obtained the pure reflectance values of the endmembers from Plot A on both June 16 and September 2, 2023. Considering that June 16 corresponds to a period just before planting, the average reflectance of 500 points was assumed to represent the pure reflectance of water (Figure 5a). On September 2, as the rice plants grew and occupied a larger proportion of the entire plot (Figure 5b), the average reflectance of 500 points on that date was assumed to represent the pure reflectance of the rice.

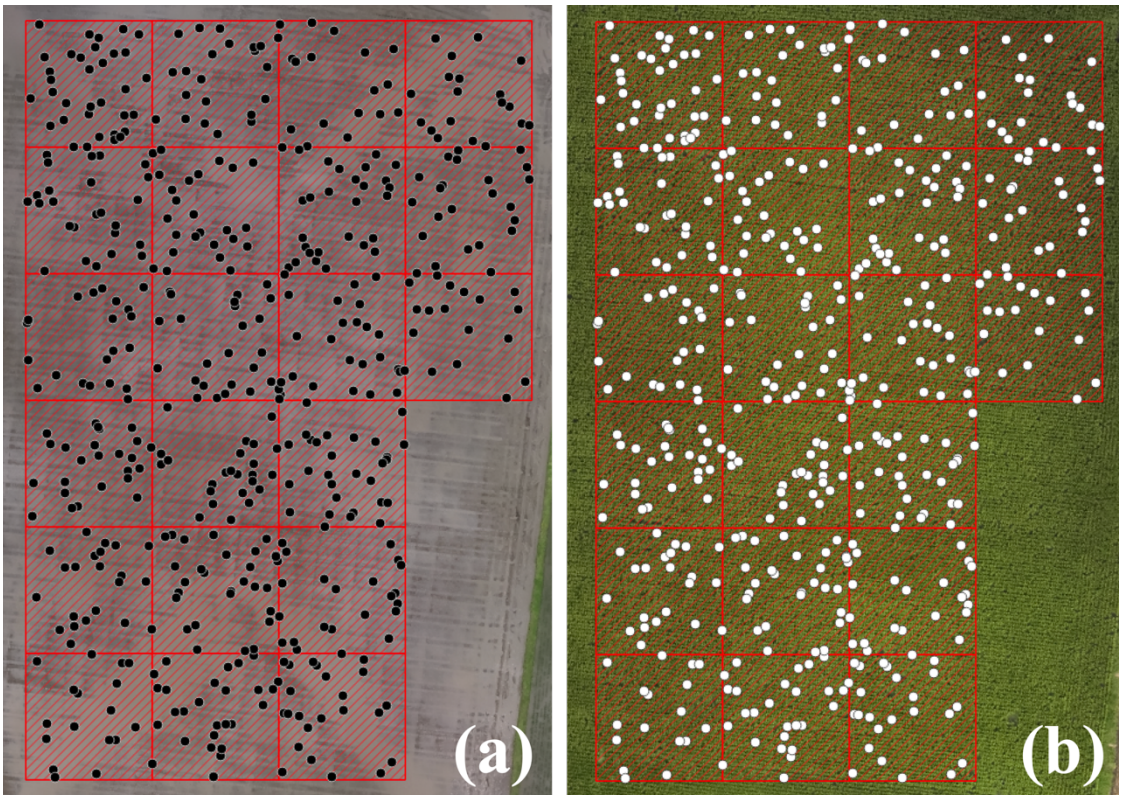

Figure 5. 500 random points on the RGB image.
(a) Endmember of water on June 16, 2023.
(b) Endmember of rice on September 2, 2023.

3.2.2 Reflectance Normalization

Considering the solar radiation conditions at the time of UAV image acquisition is crucial for accurate UAV image analysis. The construction of a reliable linear spectral unmixing model necessitates the incorporation of solar radiation considerations. Studies by Ono et al. [36,37] have demonstrated that normalizing each reflectance value using the mean value of all bands effectively suppresses sunlight and atmospheric effects. This normalization technique is commonly employed in satellite forest monitoring research and has been adapted for use in UAV monitoring in this study. Each band's reflectance was normalized by dividing it by the additive mean reflectance of all bands, aiming to mitigate differences in observation conditions (Equations (1) and (2)).

$$r_0 = r_{blue} + r_{green} + r_{red} + r_{rededge} + r_{NIR} \quad (1)$$

$$\mathrm{NR_{blue}} = \frac{\mathrm{r_{blue}}}{\mathrm{r_0}}, \mathrm{NR_{green}} = \frac{\mathrm{r_{green}}}{\mathrm{r_0}}, \ldots, \mathrm{NR_{NIR}} = \frac{\mathrm{r_{NIR}}}{\mathrm{r_0}} \quad (2)$$

In these equations,
$r_{blue}, r_{green}, r_{red}, r_{rededge}, r_{NIR}$ represents the observed reflectance of endmembers, $NR_{blue}, NR_{green}, NR_{red}, NR_{rededge}, NR_{NIR}$ represents the normalized reflectance of endmembers

3.2.3 Constrained Least Squares Method

The observed reflectance of the mixed pixel in this study can be expressed using Equation (3). The primary approaches to linear spectral unmixing methods include (i) constrained least squares, (ii) fuzzy membership methods, (iii) methods based on geometric models, and (iv) methods based on establishment models [38]. In this study, the areal fraction is computed utilizing the least-squares method, subject to the conditions $\rho_w + \rho_r = 1$, $\rho_w, \rho_r \geq 0$. All rice paddy pixels are subjected to a linear spectral mixed model (Equation (3)), and the constrained least squares method is then employed to calculate the rice plant coverage ρ_r. Additionally, a coverage map is generated as an outcome of this process.

$$\boldsymbol{NP} = \rho_w \boldsymbol{NR_w} + \rho_r \boldsymbol{NR_r} \quad (3)$$

In the provided equations,
$\boldsymbol{NP} = \left(NP_{blue}, NP_{green}, NP_{red}, NP_{rededge}, NP_{NIR}\right)$ represents the observed normalized reflectance vector of the mixed pixel, ρ_w, ρ_r represents the areal fraction of water and rice, $\boldsymbol{NR_w}, \boldsymbol{NR_r}$ represents normalized reflectance vector of water and rice, respectively.

3.3 The Estimation Model of Rice Plant Coverage

For the estimation of rice plant coverage, we developed a multiple linear regression model using Sentinel-2 images (Equation (4)). All paddy field pixels were divided into training and test data sets at an 8 to 2 ratio. The model was trained using the training data and subsequently validated with the test data. The coefficient of determination was employed for evaluating the model's performance. Additionally, validation was conducted to assess differences in Sentinel-2 products.

$$RC(i) = a_1 R_{b2}(i) + a_2 R_{b3}(i) + a_3 R_{b4}(i) + a_4 R_{b8}(i) + b \qquad (4)$$

Where, $RC(i)$ represents the average rice plant coverage calculated from UAV images at pixel i. The variables a_1, a_2, a_3, a_4, and b are regression coefficients, while (i), $R_{b3}(i)$, $R_{b4}(i)$, and $R_{b8}(i)$ denote the reflectance values of Sentinel-2 bands at pixel i.

4. Results and Discussion

4.1 Geometric Registration

Table 4 presents the geometric registration results, including correlation coefficients before and after geometric registration ($r_{original}$ and $r_{shifted}$) and the distance moved from the center ($Horizontal$ and $Vertical$) for each date and each band. The shift amount of the higher $r_{shifted}$ was adopted for each day. In other words, the shift amount of the NIR band was adopted for June 16 to July 27, and that of the green band was adopted for August 17. Notably, all correlation coefficients demonstrated improvement following the geometric registration process, with an overall enhancement rate of 6.82% (mean correlation coefficient: 0.725 to 0.773). The average absolute shift was 2.64 m horizontally and 4.08 m vertically. This result showed the effectiveness of the geometric registration process.

Table 4. Results before and after the geometric registration

Date	Band	$r_{original}$	$r_{shifted}$	Horizontal (m)	Vertical (m)
June 16, 2023	green	0.597	0.648	+1.8	−3.6
	NIR	0.817	0.915	+4.2	−4.2
June 29, 2023	green	0.420	0.428	−1.2	−2.4
	NIR	0.823	0.851	0.0	−3.6
July 14, 2023	green	0.603	0.662	−4.2	−4.2
	NIR	0.697	0.743	−3.0	−4.2
July 27, 2023	green	0.874	0.921	+0.6	−3.6
	NIR	0.867	0.935	+2.4	−3.6
August 17, 2023	green	0.797	0.830	−3.6	−4.8
	NIR	0.753	0.801	−2.4	−3.6

4.2 Normalization Evaluation

The results of the normalization process are depicted in Figure 6. Figure 6a represents the state before normalization, while Figure 6b illustrates the outcomes after normalization. Mean reflectance and standard deviation for each date are plotted. The difference in reflectance by illumination condition was considerably reduced by the normalization. In Figure 6a, it can be observed that the reflectance on June 29 is considerably higher than other dates. Conversely, Figure 6b demonstrates that this variation is effectively suppressed after normalization. During the early stages of plant growth, the reflectance in the visible light range tends to be higher due to the predominant presence of water in the pixel. As the rice plants grow, the near-infrared reflectance becomes more prominent owing to the increased fraction of rice in the pixel. This trend is clearly illustrated in Figure 6 after normalization.

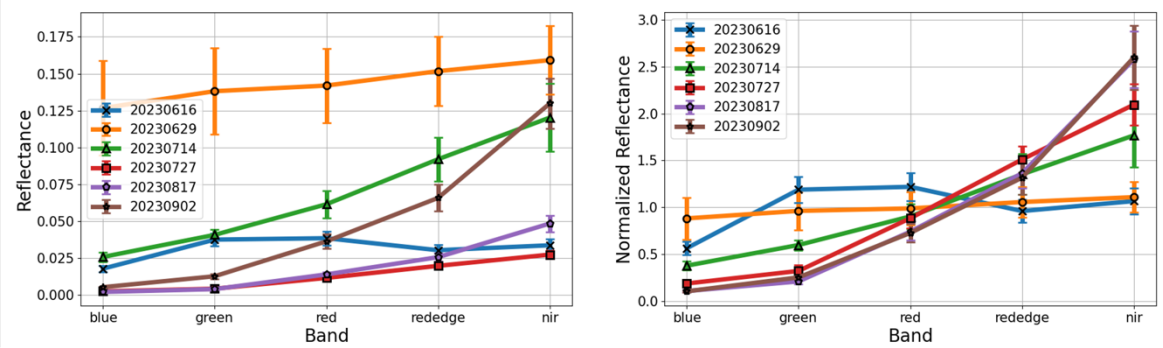

(a) **(b)**

Figure 6. Normalization results.
(a) before normalization, (b) after normalization.

4.3 Rice Plant Coverage by UAV

4.3.1 Coverage Map Derived by UAV

Figure 7 illustrates the dynamic changes in rice plant coverage within Plot A. The spatial distribution of coverage is clearly depicted, allowing for a detailed observation of rice plant growth over time. Notably, significant coverage variations were observed across different locations until July 27, capturing the nuanced changes in the field. However, after August 17, minimal changes were observed across the entire field, indicating a stable state suitable for utilization as the correct label.

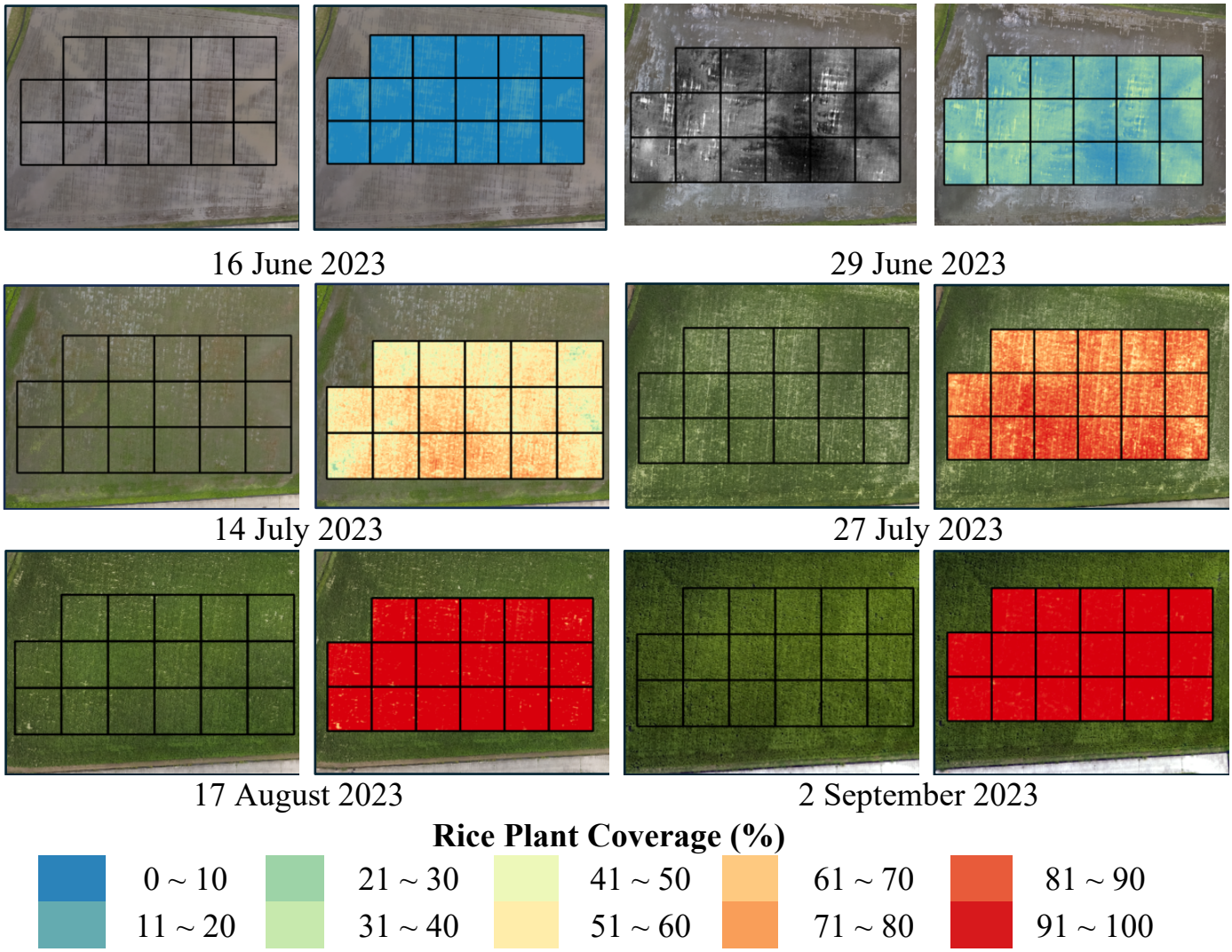

Figure 7. Rice plant coverage map of UAV images (Left: RGB image; Right: coverage map).

4.3.2 Seasonal Changes in Coverage

The variations in rice plant coverage across different plots are depicted in Figure 8. The horizontal axis represents each day passed from the planting date, while the vertical axis denotes the rice plant coverage. The plotted values represent the average coverage for each field, providing insight into the speed of rice plant growth over time.

Figure 8 illustrates a rapid growth phase for rice plants occurring between 13 and 28 days after planting. However, after 62 days, the rice plant coverage saturates. Notably, Plot B exhibits lower coverage compared to the other plots, a distinction evident in the RGB orthophotos.

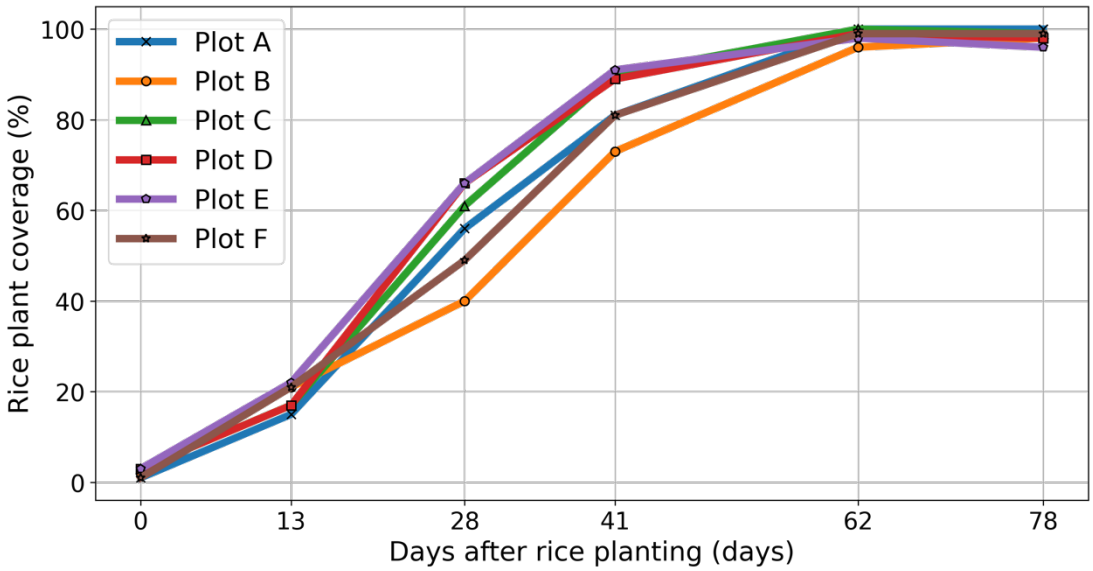

Figure 8. Seasonal coverage changes in UAV images by plots.

4.4 Rice Plant Coverage of Sentinel-2

4.4.1 Evaluation of Estimation Model

The estimated model utilizing Sentinel-2 Level-2A product, as expressed in Equation (5), underwent evaluation for its accuracy. The correlation between the estimated coverage and correct labels is visually presented in Figure 9. The horizontal axis represents the correct label in UAV images, while the vertical axis indicates the estimated coverage in Sentinel-2 images. Pixels used in the coverage analysis are plotted for each date.

Figure 9a shows the results of the Level-1C product. The coefficient of determination was found to be 0.917 for the training data and 0.917 for the test data. The RMSE values were 10.70% for the training data and 10.45% for the test data. Figure 9b shows the results of the Level-2A product. The coefficient of determination was found to be 0.945 for the training data and 0.944 for the test data. The Root Mean Square Error (RMSE) values were 9.133% for the training data and 9.039% for the test data. These results affirm the relatively high estimation accuracy of the model. However, it is noteworthy that the estimation error becomes more pronounced after the heading stage, suggesting that the model is less well-fitted during this phase.

Two potential reasons for this discrepancy are identified. Firstly, the low resolution of satellite pixels may limit their ability to represent detailed coverage appropriate to the growth stage accurately. A potential solution involves transitioning to a nonlinear regression model instead of a linear one. Secondly, the timing of image acquisition for UAV and satellite differs, and crop growth conditions can change dramatically with varying dates, especially during the growing season. A possible solution involves estimating a growth curve of coverage from UAV images, with the estimated coverage on the satellite acquisition date serving as the correct label for model estimation.

Furthermore, as shown in Figure 9a and 9b, the results for Level-1C and Level-2A products, respectively, are presented. Notably, the transition to Level-2A products led to an improvement in accuracy. This enhancement in accuracy underscores the importance of utilizing Level-2A products for more

reliable and precise estimation outcomes.

$$Coverage = -57.39R_{band2} - 458.70R_{band3} + 56.62R_{band4} + 307.07R_{band8} + 24.74 \quad (5)$$

Here, $Coverege$ represents the estimated coverage of Sentinel-2 images, while R_{band2}, R_{band3}, R_{band4}, and R_{band8} denote the Sentinel-2 reflectance values for bands 2, 3, 4, and 8, respectively.

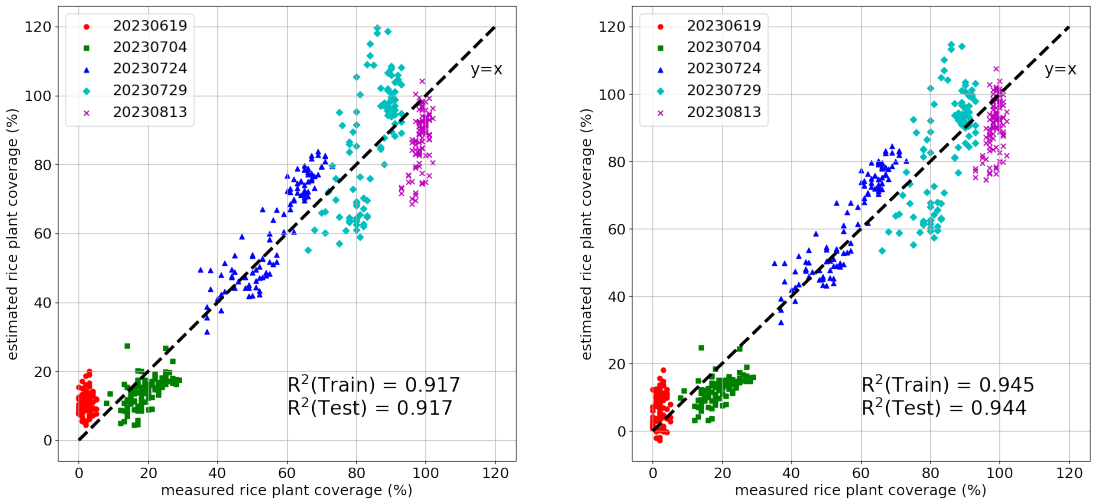

(a) **(b)**

Figure 9. Estimation coverage and correct labels.
(a) Sentinel-2 Level-1C product. (b) Sentinel-2 Level-2A product

4.4.2 Coverage Map

The dynamic changes in estimated rice plant coverage are illustrated in Figure 10. This depiction not only showcases the spatial variation in rice plant coverage but also provides a comparative reference to the UAV coverage map. Notably, plots B and F exhibit lower coverage compared to other plots. Observation of certain pixels reveals a decrease in coverage from July 29 to August 13, which may be attributed to the presence of thin clouds in the satellite data on August 13.

In an effort to mitigate cloud effects, we conducted a comparison between Sentinel-2 images for Level-2A products with atmospherically corrected surface reflectance and Level-1C with top-of-atmosphere reflectance. The results indicated that Level-2A products were superior, suppressing the impact of clouds to a certain extent. However, residual cloud effects are still evident, as depicted in Figure 10.

19 June, 2023

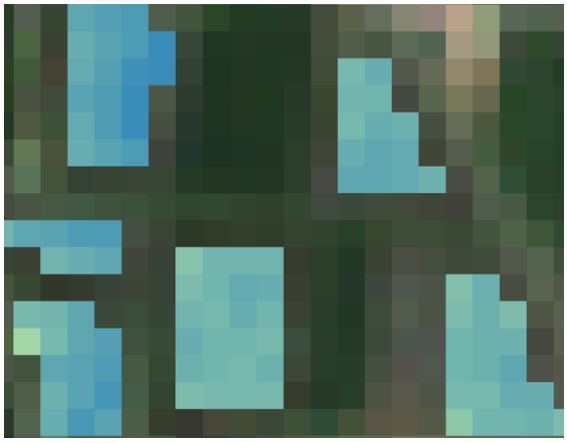

4 July, 2023

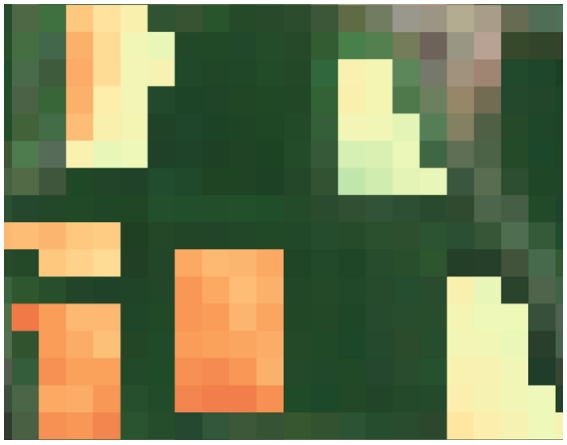

24 June, 2023

29 July, 2023

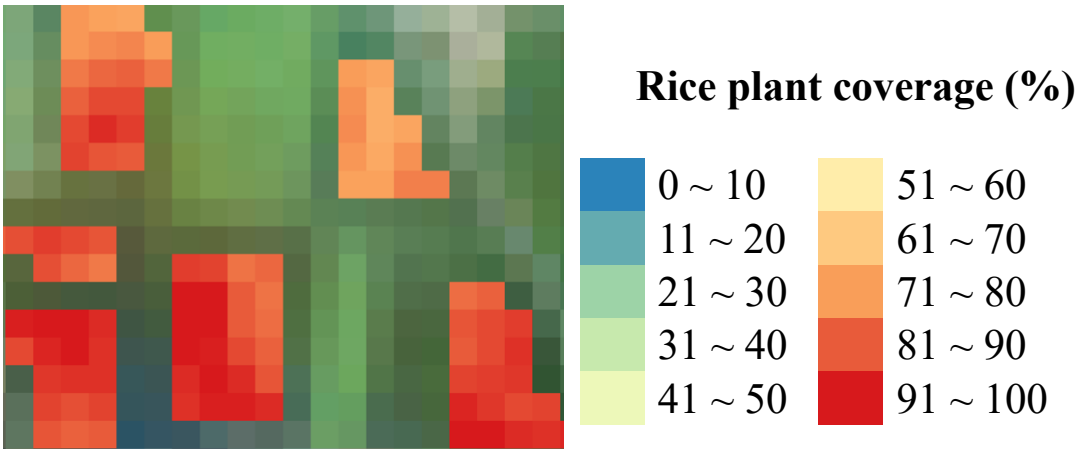

13 August, 2023

Figure 10. Rice plant coverage map of Sentinel-2 images

4.4.3 Seasonal Changes in Coverage

Figure 11 illustrates the changes in rice plant coverage across different plots. The horizontal axis represents each day elapsed from the planting date, while the vertical axis indicates the rice plant coverage. This representation enables a visualization of the speed of rice growth from the planting date.

Observationally, the estimated coverage tends to be lower than the UAV-corrected labels in almost all plots. Notably, Plot C did not reach 80% coverage even at 59 days after rice planting. Moreover, after 18 days, the disparity in coverage between plots gradually increased. This outcome emphasizes the influence of various factors on coverage estimation and highlights the importance of continuous refinement in modeling approaches.

Furthermore, the results indicate that the Level-2A product effectively mitigates the impact of clouds on Day 59. As depicted in Figure 9b, no decrease in coverage is observed, reinforcing the reliability and robustness of utilizing Level-2A products for accurate estimation despite varying atmospheric conditions.

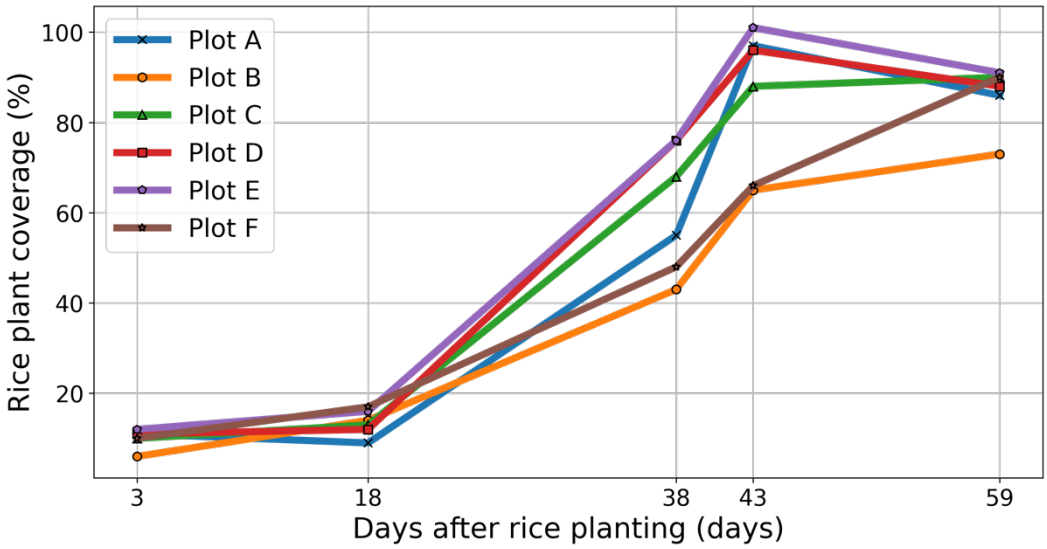

(a) Sentinel-2 Level-1C product type

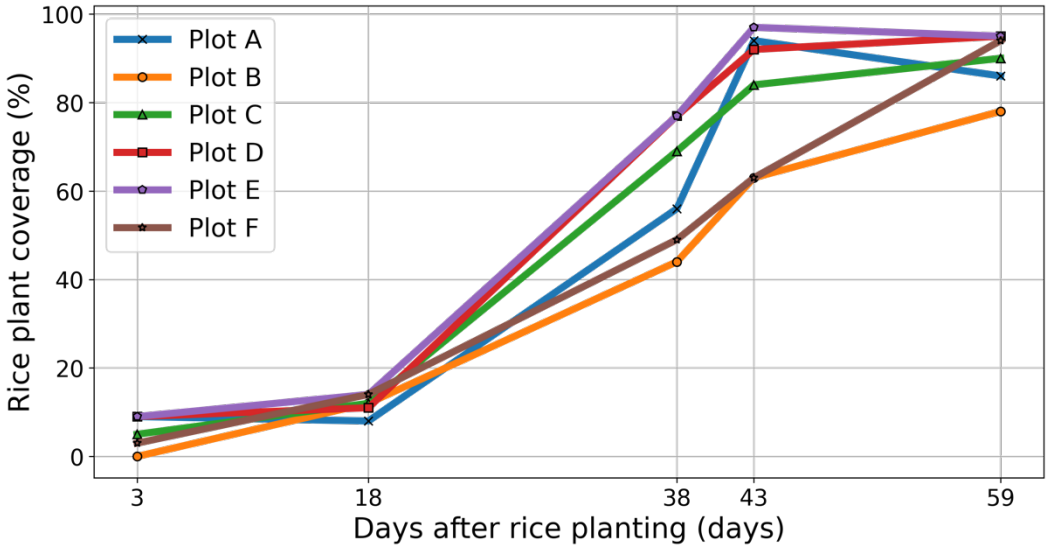

(b) Sentinel-2 Level-2A product type

Figure 11. Seasonal change in average Sentinel-2 coverage by each field

4.5 Possibility of Model Application

To assess the general applicability of the estimated model (Equation (5)), it was applied to another species, specifically "Yamada Nishiki," planted in plots G and H. The coverage changes across plots are depicted in Figure 12. The horizontal axis represents each day elapsed from the planting date, while the vertical axis indicates the rice plant coverage.

The observed coverage exhibited rapid growth on July 24 (55 days after planting). However, it is evident from Figure 13 that floating weeds significantly influenced the rice coverage. A potential solution to address this issue involves introducing a new variable into the estimation model to effectively separate rice and floating weeds. Given the challenges posed by 10-meter resolution satellite images, considering the use of higher-resolution satellite imagery is worth exploring.

Notably, Plot G displays lower coverage compared to other plots. Figure 14 illustrates a high variability in rice plant distribution within Plot G. This variability contributes to the accuracy of the coverage transition trend, showcasing the model's ability to capture nuanced variations within individual plots.

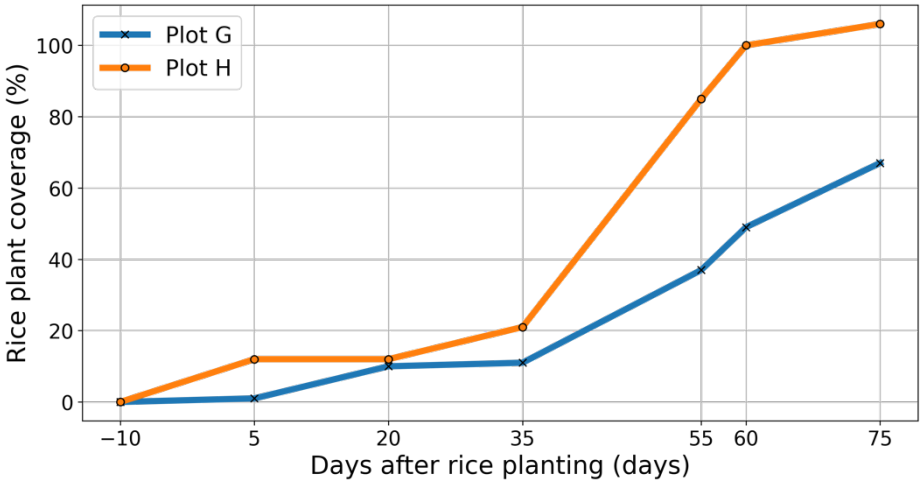

Figure 12. Seasonal coverage changes in Sentinel-2 images for “Yamada Nishiki” species

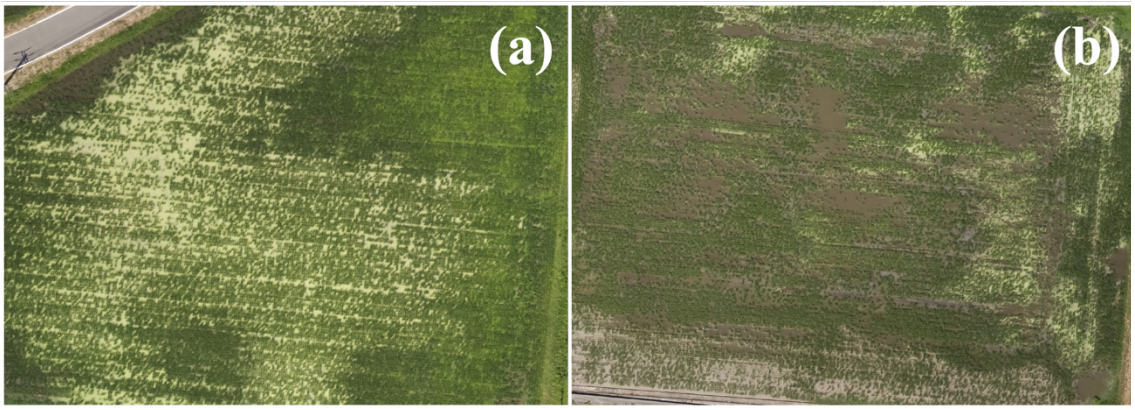

Figure 13. UAV image taken on July 29.
(a) Floating weeds on plot H, (b) rice plant variability on plot G

5. Conclusion

The primary aim of this study was to estimate rice plant coverage from satellite images. Rice plant coverage was computed from UAV-acquired images using the linear spectral unmixing method, serving as the correct label. The estimated model exhibited a coefficient of determination of 0.944, with an associated estimation error of 9.039%, achieving the targeted goal of RMSE within 10%. The coverage map offered insights into the variation among plots, and the coverage trends for each plot provided valuable information about the growth trajectory of paddy rice.

However, several challenges and issues need to be addressed, including the variability in estimation coverage during the growing season, the influence of floating weeds, and the dependency on weather conditions for satellite imagery. Our future efforts will focus on refining the analysis method to mitigate these challenges, ultimately enhancing the accuracy and stability of the estimation process.

Anticipating advancements in satellite technology, higher-resolution and more frequent satellite imagery will become available. Leveraging these evolving technologies is crucial for achieving heightened accuracy in our analysis. As articulated in the introduction, we aspire to promote the adoption of remote sensing technology within the agricultural industry, where the demand for efficient agricultural production is paramount. This pursuit aligns with the broader goal of leveraging technology to enhance and streamline agricultural practices.

Acknowledgments

This work was supported by Japan Society for the Promotion of Science (JSPS) KAKENHI grants (nos. JP21K05669, JP20K20487, and JP22H05004).

References

1. Ministry of Agriculture, Forestry and Fisheries. Report on Results of 2010 World Census of Agriculture and Forestry in Japan (in Japanese). Available online: https://www.maff.go.jp/j/tokei/census/afc/2010/houkokusyo.html (accessed on 12 March 2024).
2. Ministry of Agriculture, Forestry and Fisheries. 2020 Census of Agriculture and Forestry in Japan Census Results Report (In Japanese). Available online: https://www.maff.go.jp/j/tokei/census/afc/2020/030628.html (accessed on 12 March 2024) (in Japanese).
3. Ministry of Agriculture, Forestry and Fisheries. Summary of the Basic Plan for Food, Agriculture and Rural Areas - To Pass Japan's Food and Vigorous Agriculture and Rural Areas on the next Generation, 2020.
4. Ministry of Agriculture, Forestry and Fisheries. Current Situation and Measures for Dilapidated Farmland Available online: https://www.maff.go.jp/j/nousin/tikei/houkiti/attach/pdf/index-22.pdf (accessed on 4 March 2024) (in Japanese).
5. Ministry of Agriculture, Forestry and Fisheries. Changes in the Situation Concerning Food, Agriculture, and Rural Areas (Securing Bearers in a Declining Population) Available online: https://www.maff.go.jp/j/study/attach/pdf/nouti_housei-1.pdf (accessed on 27 January 2024) (in Japanese).
6. Agriculture, F. and F.R.C. About "Smart Agriculture Demonstration Project" Available online: https://www.affrc.maff.go.jp/docs/smart_agri_pro/smart_agri_pro.htm (accessed on 27 January 2024) (in Japanese).
7. Umemoto, M. Technological Innovation in Japanese Agriculture - Progress and Prospect-. *The Journal of Japan Economic Research* **2019**, *91*, 207–220, doi:https://doi.org/10.11472/nokei.91.207 (in Japanese).
8. Inoue, Y. Utility and Caveats of Sensing and Data Science for Smartification of Crop Production-Remote Sensing, AI, Big Data, and Phenotyping-. *Japanese Journal of Crop Science* **2023**, *92*, 91–103, doi: https://doi.org/10.1626/jcs.92.91 (in Japanese).
9. Uenishi, Y.; Nanseki, T. Analysis of Strengths and Weaknesses of

Agricultural Corporations and Their Intention to Adopt Smart Farming Technologies: A Case Study of Corporate Rice Farming. *Agricultural Information Research* **2023**, *32*, 57–65, doi: https://doi.org/10.3173/air.32.57 (in Japanese).
10. Sakamoto, T. Wide Area Monitoring of Crop Growth Using Satellite Remote Sensing Data. *Journal of the Remote Sensing Society of Japan* **2021**, *42*, 171–180, doi:https://doi.org/10.11440/rssj.41.171 (in Japanese).
11. Zhao, R.; Li, Y.; Ma, M. Mapping Paddy Rice with Satellite Remote Sensing: A Review. Sustainability 2021, 13, 1–20, doi:https://doi.org/10.3390/su13020503.
12. Mandapati, R.; Gumma, M.K.; Metuku, D.R.; Bellam, P.K.; Panjala, P.; Maitra, S.; Maila, N. Crop Yield Assessment Using Field-Based Data and Crop Models at the Village Level: A Case Study on a Homogeneous Rice Area in Telangana, India. *AgriEngineering* **2023**, *5*, 1909–1924, doi:https://doi.org/10.3390/agriengineering5040117.
13. Mukai, Y.; Rikimaru, A.; Takahashi, K.; Teraoka, N. Estimating Distribution of Growth Stages of Rice by Satellite Data. *Bulletin of Nagaoka University of Technology* **2003**, *25*, 63–67 (in Japanese).
14. Franch, B.; San Bautista, A.; Fita, D.; Rubio, C.; Tarrazó-Serrano, D.; Sánchez, A.; Skakun, S.; Vermote, E.; Becker-Reshef, I.; Uris, A. Within-Field Rice Yield Estimation Based on Sentinel-2 Satellite Data. *Remote Sens* **2021**, *13*, doi: https://doi.org/10.3390/rs13204095.
15. Zhao, Q.; Lenz-Wiedemann, V.I.S.; Yuan, F.; Jiang, R.; Miao, Y.; Zhang, F.; Bareth, G. Investigating Within-Field Variability of Rice from High Resolution Satellite Imagery in Qixing Farm County, Northeast China. *ISPRS Int J Geoinf* **2015**, *4*, 236–261, doi: https://doi.org/10.3390/ijgi4010236.
16. Inoue, Y. Analysis of Spectral Measurements in Paddy Field for Predicting Rice Growth and Yield Based on a Simple Crop Simulation Model. *Plant Prod Sci* **1998**, *1*, 269–279, doi:https://doi.org/10.1626/pps.1.269.
17. Omasa, K. Remote Sensing of Plant Functioning-Applications in Plant Diagnosis and Phenomics Researches-. *Eco-Engineering* **2014**, *26*, 51–61, doi:https://doi.org/10.11450/seitaikogaku.26.51 (in Japanese).
18. Akiyama, T.; Shibayama, M. Development of Remote Bio-Sensors for Agricultural Application. *Journal of The Remote Sensing Society of*

Japan **1985**, *5*, 77–84, doi:https://doi.org/10.11440/rssj1981.5.77.
19. Hayashi, T.; Sato, T.; Sakai, K.; Iwata, T.; Oida, T.; Mawaki, M.; Saio, K.; Ninomiya, S.; Yoshida, T. Diagnostic Approach to the Growth of Paddy Rice Using Image Analysis. I : Estimation of Leaf Area Index by Rate Vegetation Coverage. *Bulletin of the Fukui Agricultural Experiment Station* **1993**, *30*, 9–18, doi: https://doi.org/10.11501/2352790.
20. Lee, K.-J.; Lee, B.-W. Estimating Canopy Cover from Color Digital Camera Image of Rice Field. *J Crop Sci Biotechnol* **2011**, *14*, 151–155, doi: https://doi.org/10.1007/s12892-011-0029-z.
21. Jiang, J.; Atkinson, P.M.; Chen, C.; Cao, Q.; Tian, Y.; Zhu, Y.; Liu, X.; Cao, W. Combining UAV and Sentinel-2 Satellite Multi-Spectral Images to Diagnose Crop Growth and N Status in Winter Wheat at the County Scale. *Field Crops Res* **2023**, *294*, 108860, doi: https://doi.org/10.1016/j.fcr.2023.108860.
22. Schiefer, F.; Schmidtlein, S.; Frick, A.; Frey, J.; Klinke, R.; Zielewska-Büttner, K.; Junttila, S.; Uhl, A.; Kattenborn, T. UAV-Based Reference Data for the Prediction of Fractional Cover of Standing Deadwood from Sentinel Time Series. *ISPRS Open Journal of Photogrammetry and Remote Sensing* **2023**, *8*, 100034, doi: https://doi.org/10.1016/j.ophoto.2023.100034.
23. Lewis, P.H.; Roberts, B.P.; Moore, P.J.; Pike, S.; Scarth, A.; Medcalf, K.; Cameron, I. Combining Unmanned Aerial Vehicles and Satellite Imagery to Quantify Areal Extent of Intertidal Brown Canopy-forming Macroalgae. *Remote Sens Ecol Conserv* **2023**, *9*, 540–552, doi:https://doi.org/10.1002/rse2.327.
24. Kitamoto, A.; Takagi, M. Mixture Density Estimation In the Presence of Mixels. *Technical Report of Institute of Electronics, Information, and Communication Engineers (IEICE)* **1996**, *PRU95-202*, 33–40 (in Japanese).
25. Ito, T.; Fujimura, S. Estimation of Cover Area of Each Category in a Pixel by Pixel Decomposition into Categories. *Transactions of the Society of Instrument and Control Engineers* **1987**, *23*, 800–805, doi:https://doi.org/10.9746/sicetr1965.23.800.
26. Keshava, N.; Mustard, J.F. Spectral Unmixing. *IEEE Signal Process Mag* **2002**, *19*, 44–57, doi: https://doi.org/10.1109/79.974727.
27. Yuan, N.; Gong, Y.; Fang, S.; Liu, Y.; Duan, B.; Yang, K.; Wu, X.; Zhu,

R. Uav Remote Sensing Estimation of Rice Yield Based on Adaptive Spectral Endmembers and Bilinear Mixing Model. *Remote Sens* **2021**, *13*, doi:https://doi.org/10.3390/rs13112190.
28. DJI, Smart Management of Crop Growth Available online: https://www.dji.com/jp/p4-multispectral (accessed on 1 February 2024).
29. DJI, DJI GS PRO MISSION-CRITICAL FLIGHT SIMPLIFIED Available online: https://www.dji.com/ground-station-pro (accessed on 1 February 2024).
30. Micasense, Calibrated Reflectance Panel Available online: https://support.micasense.com (accessed on 1 February 2024).
31. Drusch, M.; Del Bello, U.; Carlier, S.; Colin, O.; Fernandez, V.; Gascon, F.; Hoersch, B.; Isola, C.; Laberinti, P.; Martimort, P.; et al. Sentinel-2: ESA's Optical High-Resolution Mission for GMES Operational Services. *Remote Sens Environ* **2012**, *120*, 25–36, doi: https://doi.org/10.1016/j.rse.2011.11.026.
32. Pix4D S.A PIX4Dmapper The Leading Photogrammetry Software for Professional Drone Mapping Available online: https://www.pix4d.com/product/pix4dmapper-photogrammetry-software/ (accessed on 30 January 2024).
33. Guo, Y.; Senthilnath, J.; Wu, W.; Zhang, X.; Zeng, Z.; Huang, H. Radiometric Calibration for Multispectral Camera of Different Imaging Conditions Mounted on a UAV Platform. *Sustainability* **2019**, *11*, doi: https://doi.org/10.3390/su11040978.
34. MSI ESL team Data Quality Report - L1C MSI Available online: https://sentinels.copernicus.eu/documents/d/sentinel/ompc-cs-dqr-001-12-2023-i95r0-msi-l1c-dqr-january-2024 (accessed on 8 March 2024).
35. A Free and Open Source Geographic Information System Available online: https://www.qgis.org/en/site/ (accessed on 31 January 2024).
36. Ono, A.; Fujiwara, N.; Ono, A. Suppression of Topographic and Atmospheric Effects by Normalizing the Radiation Spectrum of Landsat/TM by the Sum of Each Band. *The Journal of the Remote Sensing Society of Japan* **2002**, *22*, 318–327, doi:https://doi.org/10.11440/rssj1981.22.318 (in Japanese).
37. Ono, A.; Ono, A. Vegetation Analysis of Larix Kaempferi Using Radiant Spectra Normalized by Their Arithmetic Mean. *Journal of*

The Remote Sensing Society of Japan **2013**, *33*, 200–207, doi:https://doi.org/10.11440/rssj.33.200 (in Japanese).
38. Kitamoto, A. Remote Sensing: From Image Processing to Spatio-Temporal Processing. *The Institute of Electronics, Information and Communication Engineers (IEICE)* **2003**, 73–80.
39. Maeda, Y.; Goyotani, T.; Nishiuchi, S.; Kita, E. Yield Prediction of Paddy Rice with Machine Learning. *IPSJ Technical Report* **2018**, *2018*, 1–4 (in Japanese).
40. Sheng, R.T.-C.; Huang, Y.-H.; Chan, P.-C.; Bhat, S.A.; Wu, Y.-C.; Huang, N.-F. Rice Growth Stage Classification via RF-Based Machine Learning and Image Processing. *Agriculture* **2022**, *12*, 2137, doi:10.3390/agriculture12122137.

Appendix

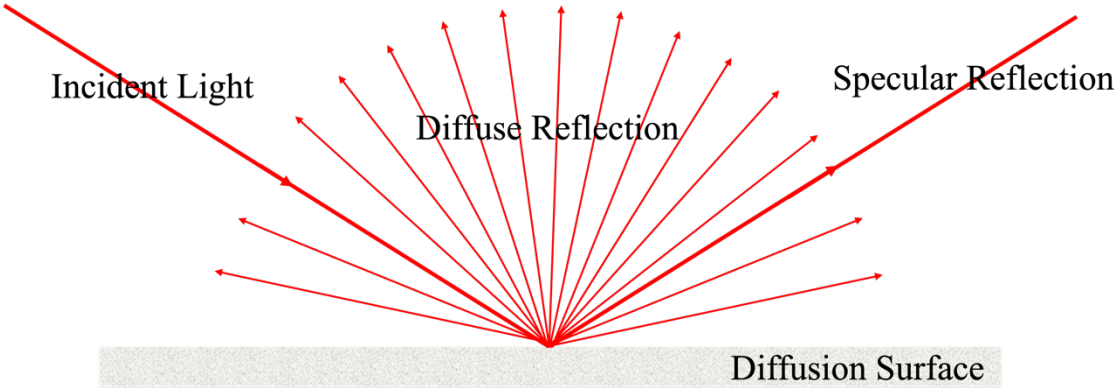

Figure A-1. Diffuse Reflection

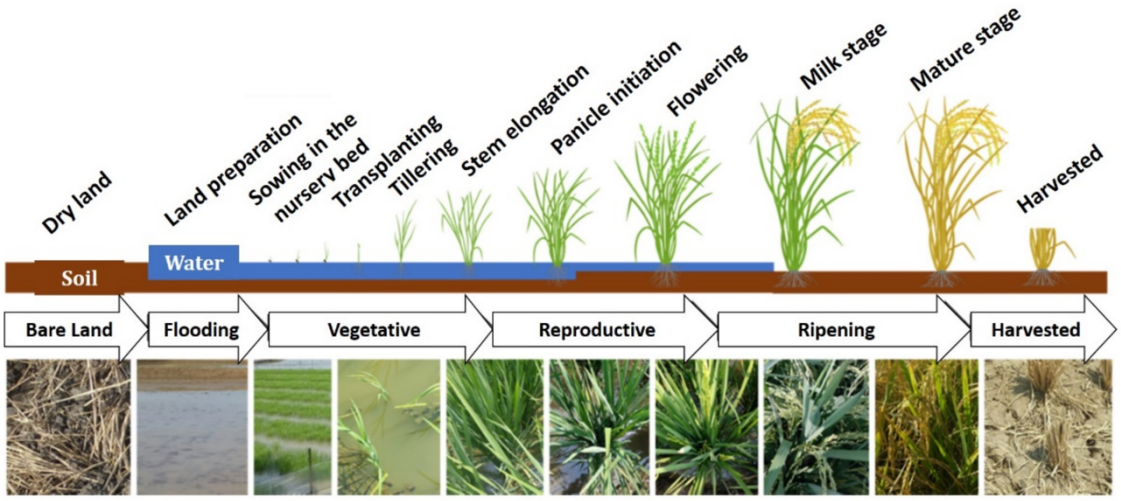

Figure A-2. Paddy Rice Growth Stages illustration [40]